Korean J. Chem. Eng., 38(1), 170-178 (2021)
DOI: 10.1007/s11814-020-0690-3

pISSN: 0256-1115
eISSN: 1975-7220

Electrochemical analysis on how structural and compositional modification of electrode affects power generation in reverse electrodialysis

Jisu Jeong*,,‡, Heajung Song*,**,‡, and Insoo Choi*,†**

*Division of Energy Engineering, Kangwon National University, 346 Jungang-ro, Samcheok 25913, Korea
**Department of Chemical Engineering, Kangwon National University, 346 Jungang-ro, Samcheok 25913, Korea
(*Received 23 July 2020 • Revised 15 September 2020 • Accepted 3 October 2020*)

Abstract−We suggest a modified Ti-based electrode for reverse electrodialysis to increase power density and retain long-term durability. Specifically, a mesh-type Ti electrode and electrochemically fabricated Pt/Ti electrode are employed in the reverse electrodialysis single cell. The electrode systems are compared in terms of power output, resistance, specific capacitance, and redox-couple reaction kinetics near the electrode surface. Among the electrodes, Pt/Ti mesh-embedded cell exhibits the highest j_{max} (−16.13 A m^{-2}) and P_{max} (−0.702 W m^{-2}). The improvement in performance is ascribed to the reduced resistance associated with heterogeneous charge transfer and to the enlarged electrochemical surface area, verified by impedance analysis, and by monitoring the capacitive behavior of the electrodes, respectively. The highest exchange current density of Pt/Ti mesh electrode is attributed to facile electron transfer and reduced power loss in the electrode compartment. Furthermore, the Pt/Ti mesh electrode allows stable operation of reverse electrodialysis for an extended time. Finally, we demonstrate the power generation of a reverse electrodialysis stack built up with multiple pairs of ion exchange membranes for potential commercial application.

Keywords: Reverse Electrodialysis, Electrode, Modification, Composition, Structure, Power Generation

INTRODUCTION

A great need has become evident for renewable energy sources that are commercially viable as well as technically feasible. Lately, salinity gradient power (SGP), where energy is generated from the reversible mixing of solutions with different salinity, has drawn enormous attention. Theoretically, when 1 m^3 of river water is mixed with the same volume of sea water, the potential energy obtainable from SGP approximates 2 MJ [1]. The energy is completely renewable, environmentally benign and, more importantly, sustainable. There are two representative and frequently discussed methods to harvest the energy from the ocean: pressure retarded osmosis (PRO) [2-4] and reverse electrodialysis (RED) [1,5,6]. The techniques can be distinguished based on the operational principle by which PRO generates electricity via a mechanical process, while RED does so via an electrochemical process. Among them, RED is regarded as more promising from a technical and economic point of view, due to the development of a more advanced membrane and the efficient conversion efficiency (~85%), respectively [7,8]. The first work by Pattle in 1957 [1], reporting the idea of RED, was stagnant, until Weinstein [9] and Lacey [10] revived interest in the RED technology, due to membrane development. Lacey performed a delicate evaluation of the economic and engineering aspect of RED [10]. At that time, it was too early to build a commercial RED power station. However, during the last decade, the prices of membrane materials have considerably lowered and plans have been made for an economically viable plant within the next few years.

In RED, there are four complementary elements: electrode, ion-exchange membrane (IEM), spacer, and solution. Various technological and scientific aspects of membrane [11-18], spacer [7,19-22], flow channel [23], and electrode system [12,24-31] have been studied. In addition, the effects of engineering parameters, such as solution concentration, temperature, and feed rate, were experimentally [32] and mathematically [33-39] investigated. Among the various aspects, membranes were mainly studied in many ways, and thus improved membranes were developed and introduced. However, the room for further improvement in membrane characteristics, such as transfer coefficient and ion exchange capacity, has become limited. Meanwhile, the electrode system where the energy conversion takes place from ionic to electric has received less attention. It has already been reported that energy loss in the electrode cannot be ignored, and when the RED is scaled up the loss becomes remarkable. Therefore, establishing a suitable and efficient electrode system is of considerable importance for the commercial application of RED.

The previous literature has suggested and described many electrode systems [27]. The early stage of research suggested primitive metal electrodes, such as Cu [5], Zn [24], and Ag/AgCl [40]. The RED cell with metal electrodes manifests the opposite electrode reaction, where one electrode grows while the other dissolves. Therefore, the feed waters should be periodically interchanged or the electrodes may be reversed to invert the direction of ionic flow, meaning that the system imposes limitations on cell design. The reversal can be avoided by employing a homogeneous redox-couple with inert electrodes, such as platinized carbon (Pt/C) [24] or Ir/Ru-coated Ti [12]. However, the system is often accompanied by gas evolution due to the side reaction of electrolyte and thus results in the loss of

†To whom correspondence should be addressed.
E-mail: ischoi@kangwon.ac.kr
‡Equally Contributed

energy. In that sense, if the current density is to be meaningful, a significant number of cells are required to overcome the cell equilibrium voltage. The state-of-the-art electrode system consists of a dimensionally stable RuIr-deposited Ti electrode with Fe^{2+}/Fe^{3+}-containing solution [26,27]. The electrode system plays a crucial role in the RED system and contributes to its practical application on a bench or pilot scale.

Our aim was (1) to improve the power output of RED by changing the structure and composition of electrode, and (2) to investigate how such changes have contributed to the improvement from an electrochemical perspective. Some reports developed new electrode systems and show performance improvement [27,28]; however, they were only limited to applying different materials and never diagnosed the causes for the improvement. The present study introduces a mesh-type electrode, from a structural point of view and compares it to a foil-type electrode. Meanwhile, the surface composition of electrode was altered through the electrodeposition method in pursuit of improving the kinetics of the electrode reaction. The electrodeposition is the technique that is widely used to sophisticatedly fabricate electrode material in the field of electrochemical conversion, storage and sensing [41,42]. The physicochemical features of the as-prepared electrodes were analyzed by various techniques. The electrodes were employed in the lab-scale RED cell and the cell performance was measured and compared accordingly. The difference and improvement in the performance were explained and supported by a variety of electrochemical analyses, including impedance spectroscopy, double-layer capacitance measurement, and potentiodynamic sweeping method. In addition, the durable operation of the RED single cell was confirmed by time-dependent cell voltage measurement. Finally, the RED stack was built using the best-performing electrode and the power generation was demonstrated. Through the experiment, we attempted to present how power losses at the electrodes could be minimized by employing modified Ti-based electrodes for the RED and tried to explain how and why it works. We hope that the study provides insight into designing and fabricating a high-performance, durable, and electrochemically active electrode for RED.

MATERIALS AND METHODS

1. Fabrication of the Lab-scale RED Cell

Fig. 1 a shows a schematic of a RED single cell and the flow of

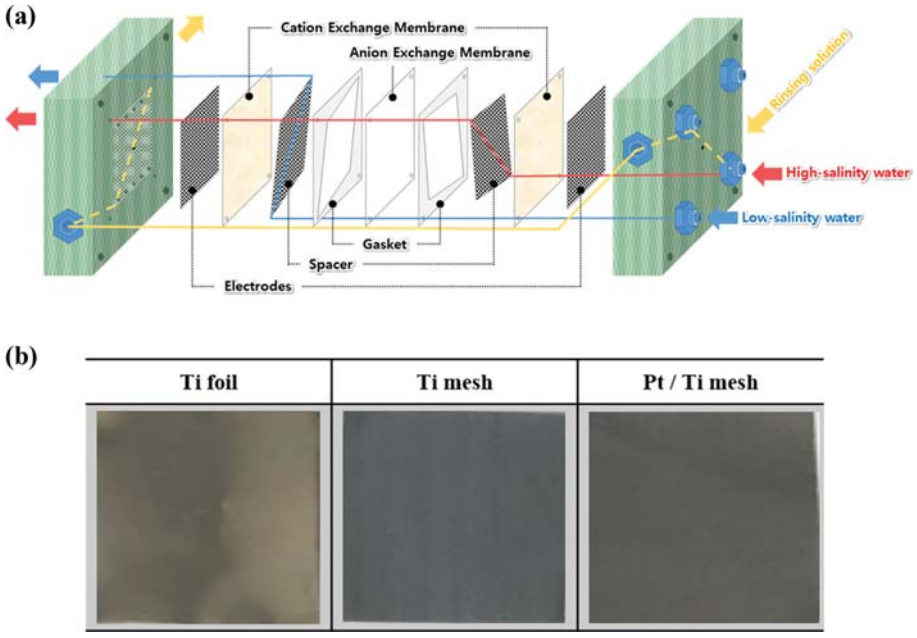

Fig. 1. (a) Schematic of a RED single cell including all compartments, (b) optical images of the various electrodes used in this study.

Table 1. Specification of the cation and anion exchange membranes used in the present study

	CMV-N (cation exchange membrane)	AMV-N (anion exchange membrane)
Counter ion	Na^+	Cl^-
Thickness (μ)	100	100
Area resistance (Ω cm^2)	2.0	2.0
Transport number	t_{Na+}>0.97	t_{Cl-}>0.94
Ion exchange group	Sulfonic	Quaternary ammonium
Ion exchange capacity (meq g^{-1})	1.5-1.8	1.85±0.04

all solutions. Two types of IEMs were purchased and used for Na^+ and Cl^- transport in this experiment: CMV-N and AMV-N for cation exchange membrane (CEM) and anion exchange membrane (AEM), respectively (Selemion™, Asahi Glass Co. Ltd., Japan). Table 1 provides the specification of the membranes. The single cell consisted of alternating CEM and AEM (5 cm×5 cm, thickness=120 μm), which were separated by Ti woven spacer (4.2 cm×5.3 cm, thickness=200 μm). The spacer was cut into rhombic shape and embedded to guide the water flow via hole (Φ=2 mm) from one end to the other. The spacer was surrounded by 320 μm thick Teflon gasket to complete the water compartment between membranes. In addition, the silicon gasket (thickness=500 μm) was placed to prevent leakage of solution. The membranes, gaskets, separators, and electrodes were assembled in sequence and backed by homemade Epoxy endplates (7 cm×7 cm). Pt wire (99%, Sigma-Aldrich, Φ=1 mm) was in contact with the electrodes and used as a connecting line to the outer circuit.

2. Preparation of Electrodes

Three electrodes were prepared and evaluated for comparison in this study: Ti foil (99.7%, 250 μm, Sigma Aldrich), Ti mesh (100 μm, 100 mesh, based on ASTM standard, Nilaco Co. Ltd, Japan), and Pt-deposited Ti mesh (Pt/Ti mesh). The Pt/Ti mesh electrode was electrochemically fabricated by depositing Pt on Ti mesh. In detail, the deposition proceeded in a three-electrode cell, where Ti mesh, Pt wire, and saturated calomel electrode (SCE) were used as working, counter, and reference electrode, respectively. Pt was electro-deposited on Ti mesh at −0.4 V_{SCE} for 0.5 h in 5 mM $H_2PtCl_6 \cdot 6H_2O$+0.05 M H_2SO_4. The electrode was dried and thermally treated in vacuum oven at 100 °C overnight. The effective geometrical area of all electrodes was 9 cm^2. The micro-structure and surface composition of the electrodes were analyzed by field emission scanning electron microscopy (FE-SEM, Merlin Compact, ZEISS). Fig. 1(b) shows the photo images of each electrode used in this study.

3. Operation of the Lab-scale RED Cell

The feed water solutions were prepared by dissolving sodium chloride (NaCl, reagent grade, Sigma-Aldrich) in de-ionized water. In this study, the concentration of low-salinity water (C_L) and high-salinity water (C_H) was fixed at (0.5 and 30) g L^{-1}, respectively. Both low- and high-salinity solutions were supplied with 5 mL min^{-1} to inlet (Φ=2.2 mm) of the RED cell by peristaltic pump (EMP-600A, EMS-Tech). The brackish water, which was generated after the mixing, was discarded, in order to maintain the salinity ratio during operation. The redox couple-containing solution, also called electrode rinse solution, consisted of 1 M NaCl mixed with 0.05 M $K_4Fe(CN)_6$ (Sigma-Aldrich)+0.05 M $K_3Fe(CN)_6$ (Sigma-Aldrich). The rinse solution flowed through the compartments adjacent to the electrodes and was continuously circulated by the pump in a closed loop at a flow rate of 3.6 mL min^{-1}. Our previous study had already optimized the concentration of feed water solutions and the flow rates of all solution for the best performance [32].

4. Electrochemical Measurement

The performance of RED cells was measured by potentiostat (PGSTAT302N, Autolab). The open circuit voltage (OCV) of the RED cell was measured after 100 s for equilibration and the operating voltage was measured by galvano-dynamic operation with a current rate of 0.1 mA s^{-1} until the voltage decayed to zero. From the measurement, both j-V and j-P plots were obtained. The durability of the RED cells was investigated by conducting chronopotentiometry at −0.5 mA cm^{-2} for 4 h. In a RED stack, up to 14 pairs of IEM were arrayed alternately between electrodes.

The electrochemical impedance spectroscopy (EIS) measurement was performed in the frequency range (10^3-10^{-1}) kHz when the cell resides at OCV state and the amplitude was set to be 1 mV. The electrochemical double-layer capacitance (EDLC) measurement of the as-prepared electrodes was conducted in 0.1 M KOH with different scan rates ranging (10-100) mV s^{-1}. Prior to the measurement, cyclic voltammetry of each electrode in the same electrolyte was conducted to obtain the potential range where the double-layer charging current appeared. The potentiodynamic sweep on the as-prepared electrodes was performed by sweeping voltage from (−0.6-1.0) V_{SCE} at 1 mV s^{-1} in 1 M NaCl mixed with 0.05 M $K_4Fe(CN)_6$+0.05 M $K_3Fe(CN)_6$. Both experiments were conducted in the three-electrode cell, where the calomel electrode and Pt wire were used as reference and counter electrode, respectively.

RESULTS AND DISCUSSION

1. Characterization of Electrodes

FE-SEM analysis was performed to investigate the micro-structure and surface morphology of the as-prepared or manufactured electrodes. Fig. 2 shows the results. Figs. 2(a) and (b) show images of the commercial Ti foil electrode with low and high magnification, respectively. Overall, the Ti foil displays a relatively flat surface with few cracks and unobtrusive edges. Fig. 2(c) shows the

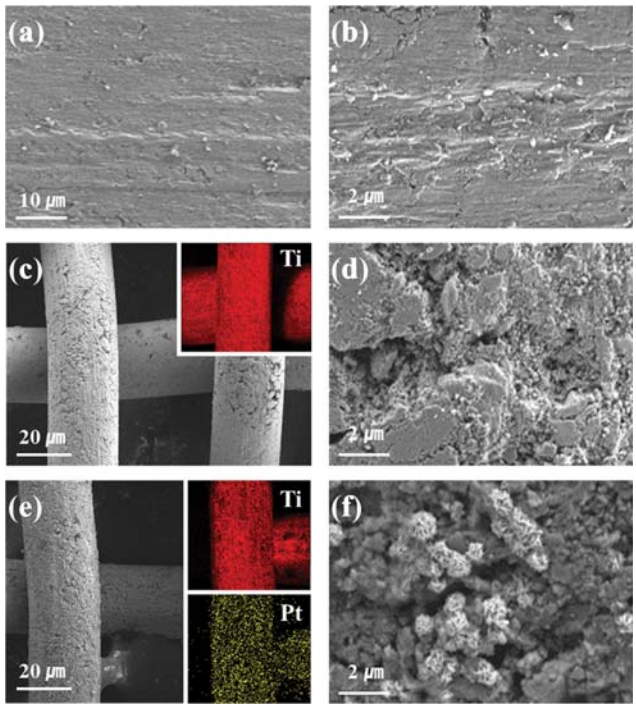

Fig. 2. FE-SEM images of (a) and (b) Ti foil, (c) and (d) Ti mesh, and (e) and (f) Pt/Ti mesh electrode. Insets in (c) and (e): corresponding EDS elemental mapping.

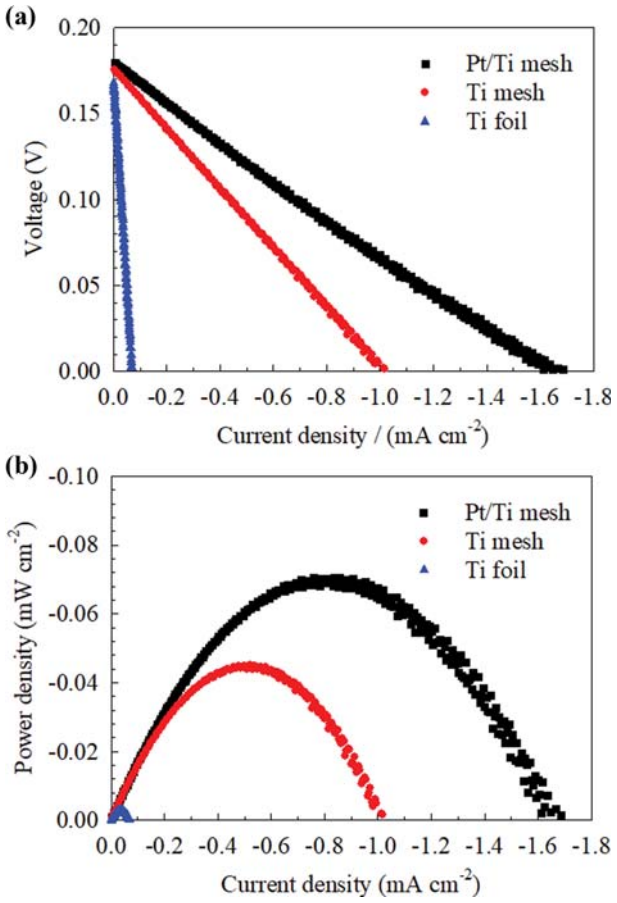

Fig. 3. (a) j-V plots, and (b) j-P curves of RED single cells embedded with Ti foil (blue triangle), Ti mesh (red circle), and Pt/Ti mesh (black square) electrode.

surface of commercial Ti mesh electrode, and EDS elemental mapping reveals the composition (inset of Fig. 2(c)). As seen in the high magnification image of Fig. 2(d), Ti mesh contains large and deep crack unlike Ti foil, suggesting that the surface retains high roughness and specific surface area. The Pt/Ti mesh electrode prepared via the electrodeposition of Pt does not demonstrate huge difference in surface morphology from Ti mesh in the image of low magnification. The EDS elemental mapping shows that Pt is evenly electrodeposited on the surface of Ti mesh (inset of Fig. 2(e)). Fig. 2(f) presents the round-type Pt nano-particulates on the Ti mesh, forming a three-dimensional network.

Table 2. Performance of RED single cell with different electrodes: OCV, j_{max}, P_{max}, and R_{cell}

	Ti foil	Ti mesh	Pt/Ti mesh
OCV (V)	0.169	0.175	0.179
j_{max} (mA cm^2)	−0.0695	−1.001	−1.613
P_{max} (mW cm^{-2})	−0.00297	−0.0449	−0.0702
R_{cell} (Ω)	270.2	19.43	12.33

2. Operation of the Lab-scale RED Cell

The as-prepared electrodes were mounted in the RED cell containing a pair of IEMs and the performance of the unit cell was measured. For the first 100 s of equilibration, stable OCV was confirmed and the voltage profile with respect to current density (j-V plot) was obtained from galvano-dynamic operation at 0.1 mA s^{-1} (Fig. 3(a)). Moreover, Fig. 3(b) shows the j-P curves that could be derived from Fig. 3(a). The stable voltage during application of a current, in combination with the OCV, reveals the total internal cell resistance (R_{cell}). Table 2 summarizes the performance of RED single cells according to the type of electrode, with OCV, j_{max}, P_{max}, and R_{cell} as indicators. The OCV of the RED cell increases in the order of Ti foil, Ti mesh, and Pt/Ti mesh. Theoretically, the cell voltage is the sum of the Nernst potential difference over the CEM and over the AEM and is an increasing function of the permselectivity of membrane and the ratio of activity of the solution [32]. Although the structure and composition of the electrode is not a determining factor on OCV, the OCV of Pt/Ti mesh is the highest (0.179 V) and is quite close to the theoretical OCV value (0.182 V) under the current circumstance. From this, it can be concluded that the ion exchange through the membrane and the reversible process near the electrode surface occur in the Pt/Ti-embedded RED cell at the most ideal extent. Here j_{max} refers to the maximum current value that the RED cell can generate. For Ti foil, j_{max} was limited to −0.0695 mA cm^{-2}, where the negative sign indicates that the current was extracted from the cell using electric load. When the mesh type electrode was applied to the cell, j_{max} increased by approximately 14.4 times. The surface-altered Pt/Ti mesh electrode helped increase j_{max} by 23.5 times. The RED cell with Pt/Ti

Table 3. The power density (in mW/cm^2) from other studies and in this study with similar experimental condition

Author	Year	Power density	Note
Weinstein et al. [9]	1976	0.0170	1 g L^{-1}/30 g L^{-1}
Jagur-Grodzinski et al. [24]	1986	0.0408	0.468 g L^{-1}/32.8 g L^{-1}
Turek et al. [25]	2007	0.0460	0.56 g L^{-1}/35.4 g L^{-1}
Dlugolecki et al. [19]	2009	0.0760	1 g L^{-1}/30 g L^{-1}
Vermass et al. [13]	2011	0.0790	1 g L^{-1}/30 g L^{-1}
Daniilidis et al. [43]	2014	0.380	100 μm-spacer, 0.01-5 M
Zhu et al. [44]	2015	0.220	0.351 g L^{-1}/35.1 g L^{-1}
Choi et al. [32]	2016	0.0846	0.5 g L^{-1}/30 g L^{-1} rinse soln. flow rate=5 ml min^{-1}
Jeong et al. (this study)	2020	0.0702	0.5 g L^{-1}/30 g L^{-1}

electrode exhibited the best performance, which could be reaffirmed from P_{max}, the maximum power density that the cell produces. The measured P_{max} was comparable to the values reported by other research groups as given in Table 3. R_{cell} can be calculated by the slope of the j-V plot and it decreased in the order Ti foil>Ti mesh>Pt/Ti mesh. The trend in R_{cell} indicated that the use of the Pt/Ti electrode improved the resistance associated with the faradaic process.

The increased performance in lab-scale RED by either adopting the mesh structure or applying the Pt deposition is somewhat straightforward and easily expected. However, it has to be explained how this enhancement is related to the electrode's electrochemical properties in order to rationalize the use of such an advanced electrode system.

3. Electrochemical Investigation of Electrodes

Basically, the cell resistance (R_{cell}) consists of the ohmic resistance (R_{ohm}), heterogeneous ionic or electric transport resistance (R_{HT}), and the boundary layer resistance (R_{BL}). R_{BL} is non-ohmic and is caused by concentration polarization near the membrane surface [32]. R_{ohm} can be further divided into the contributions from the membrane pair ($R_{membrane}=R_{CEM}+R_{AEM}$), spacer ($R_{spacer}$), and the concentration of high and low salinity solution (R_H+R_L):

$$R_{cell}=R_{membrane}+R_{spacer}+R_H+R_L+R_{HT}+R_{BL} \quad (1)$$

The electrochemical impedance analysis enables R_{ohm} and R_{HT} to be measured, which leaves R_{BL} when R_{ohm} and R_{HT} are subtracted from R_{cell}. If all the conditions except the electrode are the same, it is assumed that there is no net change in $R_{membrane}$, R_{spacer}, R_H, and R_L, and therefore any change in the impedance is attributed to the change in heterogeneous charge transfer resistance. To confirm the resistance improvement by adopting the structure and composition modification of the electrode, EIS analysis was conducted. Fig. 4(a) shows the Nyquist plots of each electrode. EIS fitting based on the corresponding equivalent circuit [45] provided the information on the individual resistance, of which Fig. 4(b) shows the values. For R_{ohm}, there was no significant discrepancy in resistance between Ti foil (4.27 Ω) and Ti mesh (4.38 Ω). Pt/Ti mesh had somewhat greater resistance (4.78 Ω) than the previous ones, which was ascribed to the formation of new interface through electrodeposition and to the increased thickness. It is noteworthy that a sharp decrease in R_{HT} was observed in Ti mesh, compared to Ti foil (201.6≫13.08) Ω This was because the mesh electrodes were structurally facile for the fluid to flow out-of-plane, thus facilitating the ion transfer to the electrode surface. R_{HT} was further reduced in Pt/Ti mesh electrode, as it was easier to transfer charge on a highly conductive Pt surface, thereby minimizing activation over-potential. The different activation over-potential from Ti and Pt/Ti mesh electrode was reflected by OCV values in Table 2. This claim will be explained and supported with more details in the next paragraph. As regards R_{BL}, it was negligible for two mesh-type electrodes while R_{BL} occupied a relatively large portion in R_{cell}. The small R_{BL} was assumed to be due to the reduced thickness of boundary layer near the electrode surface as a result of the formation of permeable flow through the holes in the mesh-type electrodes. In addition, the electrode surface of the mesh-type electrode was rather rough, compared to that of the foil electrode, as seen in

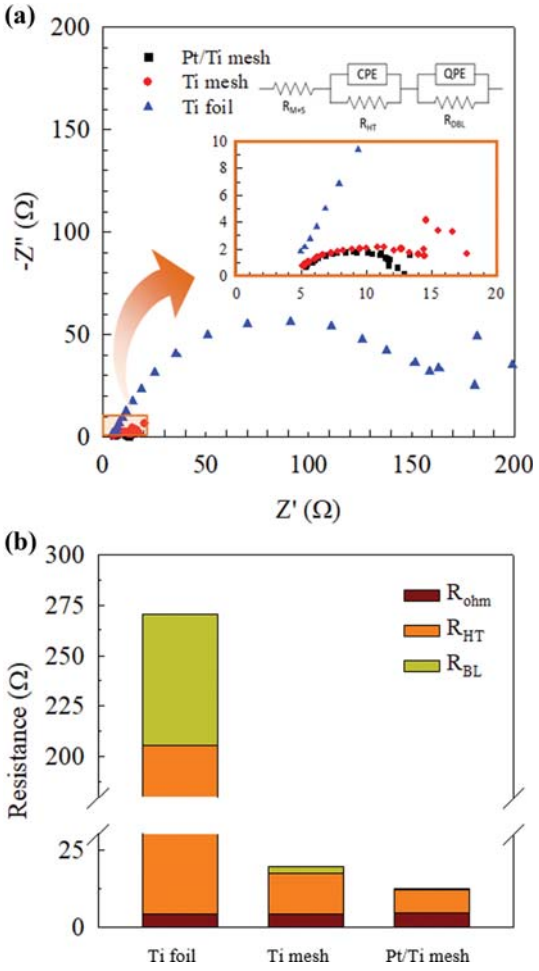

Fig. 4. (a) Nyquist plots obtained by EIS measurement of RED single cells embedded with Ti foil (blue triangle), Ti mesh (red circle), and Pt/Ti mesh (black square) electrode, (b) individual resistances obtained from fitting the Nyquist plots.

Figs. 2(c)-(f). Experimental studies on metal surfaces have reported increased hydrophilicity as the roughness increases [46,47]. Enhanced hydrophilicity of the surface should facilitate interfacial contact with the electrolyte, which also could contribute to lower the thickness of the boundary layer.

The reduced R_{HT} from the mesh-type electrode can be attributed not only to the aspects taking the fluid flow into account but also to an increase of active area. To support this, EDLC was measured by performing cyclic voltammetry in 0.1 M KOH using the three-electrode apparatus, thereby analyzing the capacitive behavior of Ti foil, Ti mesh, and Pt/Ti mesh (Figs. 5(a)-(c)). It is possible to obtain the specific capacity of each electrode from the slope of the capacity charging current with respect to scan rate. The capacitance of each electrode is proportional to its surface area, from which the electrochemical active surface area is reflected. The result showed that the specific capacitance increased in the order Ti foil (17.3 μF cm^{-2}), Ti mesh (307 μF cm^{-2}), and Pt/Ti mesh (382 μF cm^{-2}). Therefore, it can be concluded that the very large active surface area of the mesh-type electrode resulted in the drastic reduction in resistance. Meanwhile, the fact that the specific capac-

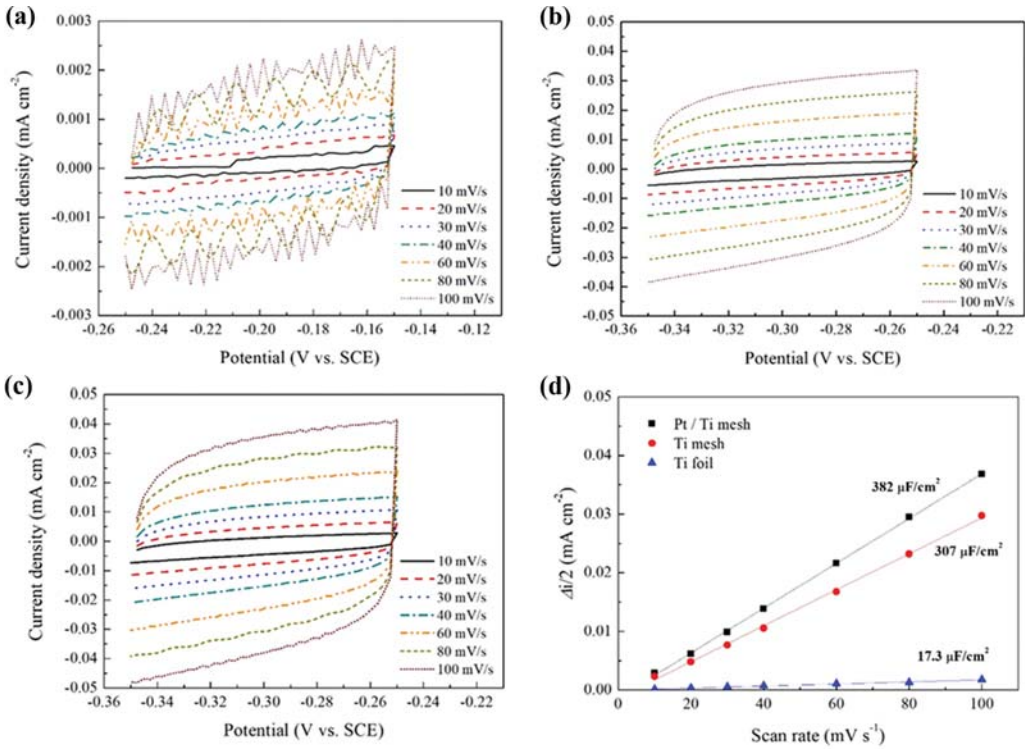

Fig. 5. Electrochemical double-layer capacitance measurement of (a) Ti foil, (b) Ti mesh, and (c) Pt/Ti mesh. (d) The capacitive charging current in the electrodes against the scan rate.

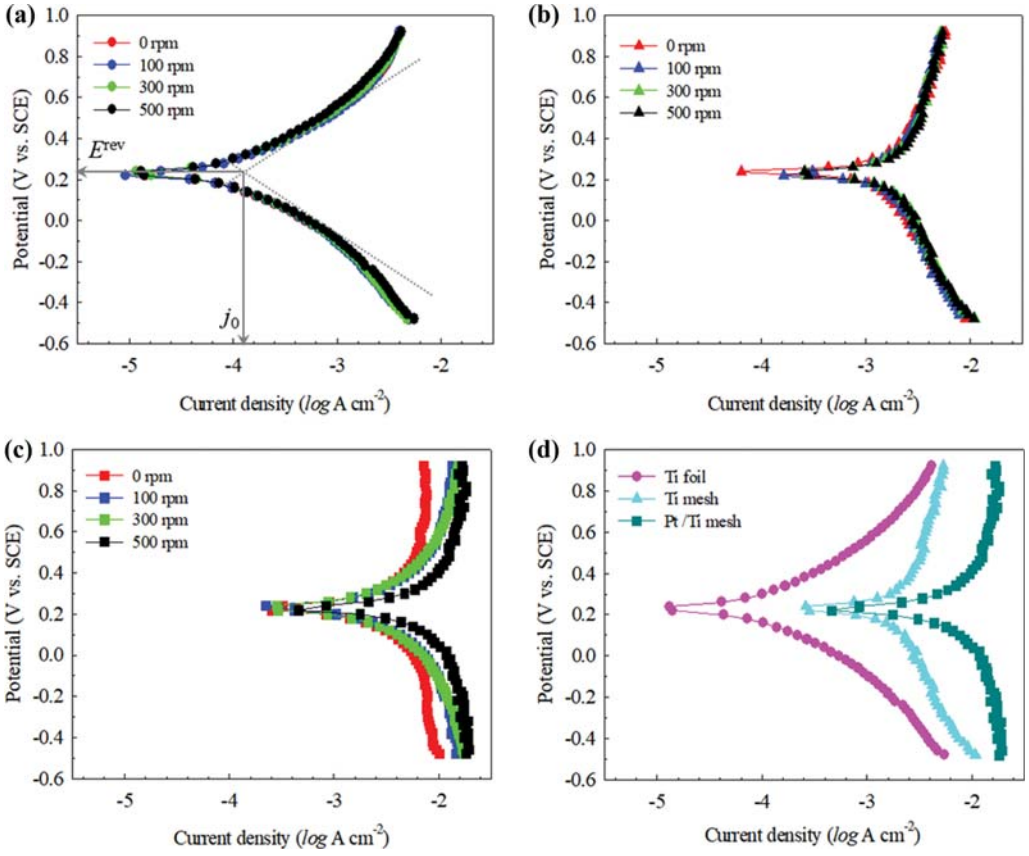

Fig. 6. Potentiodynamic sweep of the various electrodes at 1 mV s^{-1}, and at 298 K; (a) Ti foil, (b) Ti mesh, (c) Pt/Ti mesh, (d) all electrodes at 500 rpm. The dashed lines represent the Tafel behavior that gives exchange current density, j_0, and the reversible potential, E^{rev}.

itance of Pt/Ti mesh was even greater than that of Ti mesh, despite Ti being more capacitive than Pt, meant that the specific surface area of Pt/Ti mesh was high enough. The previous comparison of Figs. 2(d) and f supports this conclusion.

The generation of current in the RED cell is ultimately determined by how well the electrode converts the ionic current to electric current. For the sense, consider the kinetic of Fe^{2+}/Fe^{3+} redox reaction in electrode rinse solution near the electrode surface. Fig. 6 presents the results of the potentiodynamic sweep of the different electrodes when they were exposed to the $K_4Fe(CN)_6/K_3Fe(CN)_6$+ 1 M NaCl at 298 K. The potential-current relationship provides the kinetic parameters of the electrode reaction. For the one-electron transfer reaction, an approximate Tafel slope of 118 mV dec^{-1} is expected. We therefore adjusted the two lines of each log j vs. E figure of Figs. 6(a)-(c) in such a manner that they crossed each other at the constant potential when j became zero. By doing this, we were able to make a rough estimation of the exchange current density (j_0) of the electrodes. The sweeping was done for multiple scan rate ranging (0-300) rpm, in pursuit of finding the limiting current density. Furthermore, the potential where two lines crossed was assigned to reversible potential (E^{rev}). Table 4 summarizes the results from the potentiodynamic sweep of the electrodes. Fig. 6(d) compares the sweeping curves from three different electrodes. At 500 rpm, the j_0 of Pt/Ti mesh was 4.3- and 45.7-times greater than that of Ti mesh and Ti foil, respectively. Considering that an active interface gives a high exchange current density, normally implying small activation over-potential and small loss of energy, Pt/Ti mesh outperformed the others. E^{rev} of Fe^{2+}/Fe^{3+} remained near 0.22 V, regardless of the rpm and type of electrode.

To verify the sustainable operation of the RED cell embedded with the structure and composition modified electrodes, the chronopotentiometry of RED cell was conducted at −0.5 mA cm^{-2} for 4 h. Fig. 7 shows the results of the experiment that was done for Pt/Ti mesh and Ti mesh. Ti foil was excluded from the durability test, due to the rapid voltage drop during the constant current operation. For Ti mesh, the initial voltage was 0.1053 V and after 4 h of operation, it decreased to 0.0899 V, manifesting a decay rate of −14.6%. In contrast, the voltage of the cell with Pt/Ti mesh changed from (0.1284 to 0.1227) V and the decay rate was limited to only −4.44%. The difference in the durability is attributed to the anti-oxidation ability of metals. Even though Ti is one of the highest noble metals in the galvanic series, it may oxidize in the rinse solution. Meanwhile, Pt is the hardest to oxidize and thus the RED cell with Pt/Ti electrode maintained its power output. From the observation, plating Ti mesh with Pt clearly improved the durability of the cell, as well as the kinetic characteristic of the electrode itself.

Table 4. Results from the potentiodynamic sweep of various electrodes: exchange current density (j_0), limiting current density (j_{lim}), and reversible potential (E^{rev})

Parameter	rpm	Ti foil	Ti mesh	Pt/Ti mesh
J_0 (log A cm^{-2})	0	−3.90	−2.61	−1.93
	100	−3.81	−2.76	−2.23
	300	−3.75	−2.72	−2.17
	500	−3.69	−2.67	−2.03
J_{lim} (log A cm^{-2})	0	−2.39	−2.05	−1.71
	100	−2.32	−2.10	−1.97
	300	−2.32	−1.95	−1.82
	500	−2.25	−1.95	−1.74
E^{rev} (V)	0	0.239	0.239	0.219
	100	0.219	0.223	0.228
	300	0.239	0.243	0.243
	500	0.219	0.219	0.222

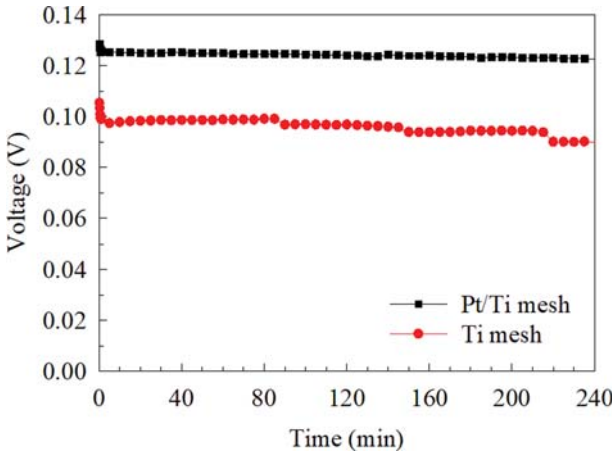

Fig. 7. Chronopotentiometry of RED single cells embedded with Ti mesh (red circle) and Pt/Ti mesh (black square) electrode at −0.5 mA cm^{-2} for 4 h.

The RED stack including the best performing Pt/Ti electrodes was manufactured and its performance was evaluated. The stack was built by sequentially stacking the CEM and AEM (1 pair of IEMs=1 cell, up to 14 cells), and Fig. 8 shows the results of the OCV, j-V, and j-P. In all stacks, OCVs were maintained over time (Fig. 8(a)). Furthermore, the tendency in OCV showed a first-order linear relationship with the number of cells in the RED stack (Fig. 8(b)). As the number of cells in the stack increased, j_{max} and P_{max} tended to gradually increase, while R_{cell} was found to increase due to the increased number of membranes and spacers. The RED stack containing 14 cells generated a maximum power density of about −2.18 mW cm^{-2}. Using the current generated from the RED stack with 14 cells (Fig. 8(e)), we illuminated 18 LED lamps simultaneously, thereby confirming the practical power-producing capability of the RED stack with Pt/Ti mesh electrodes (Fig. 8(f)).

CONCLUSION

We have modified the structure and composition of the Ti-based electrode. The as-prepared electrodes were employed in a lab-scale RED single cell or stack to improve the power output and durability. From a structural perspective, Ti mesh was replaced with Ti foil. Furthermore, Ti mesh was electrochemically modified by plating Pt thereon, forming Pt/Ti mesh, to investigate the effect of electrode surface composition on the electrode kinetics. The FE-SEM along with the EDS analysis confirmed the clear difference in micro-structure between mesh and foil type electrode and the successful modification in composition. The actual operation of RED

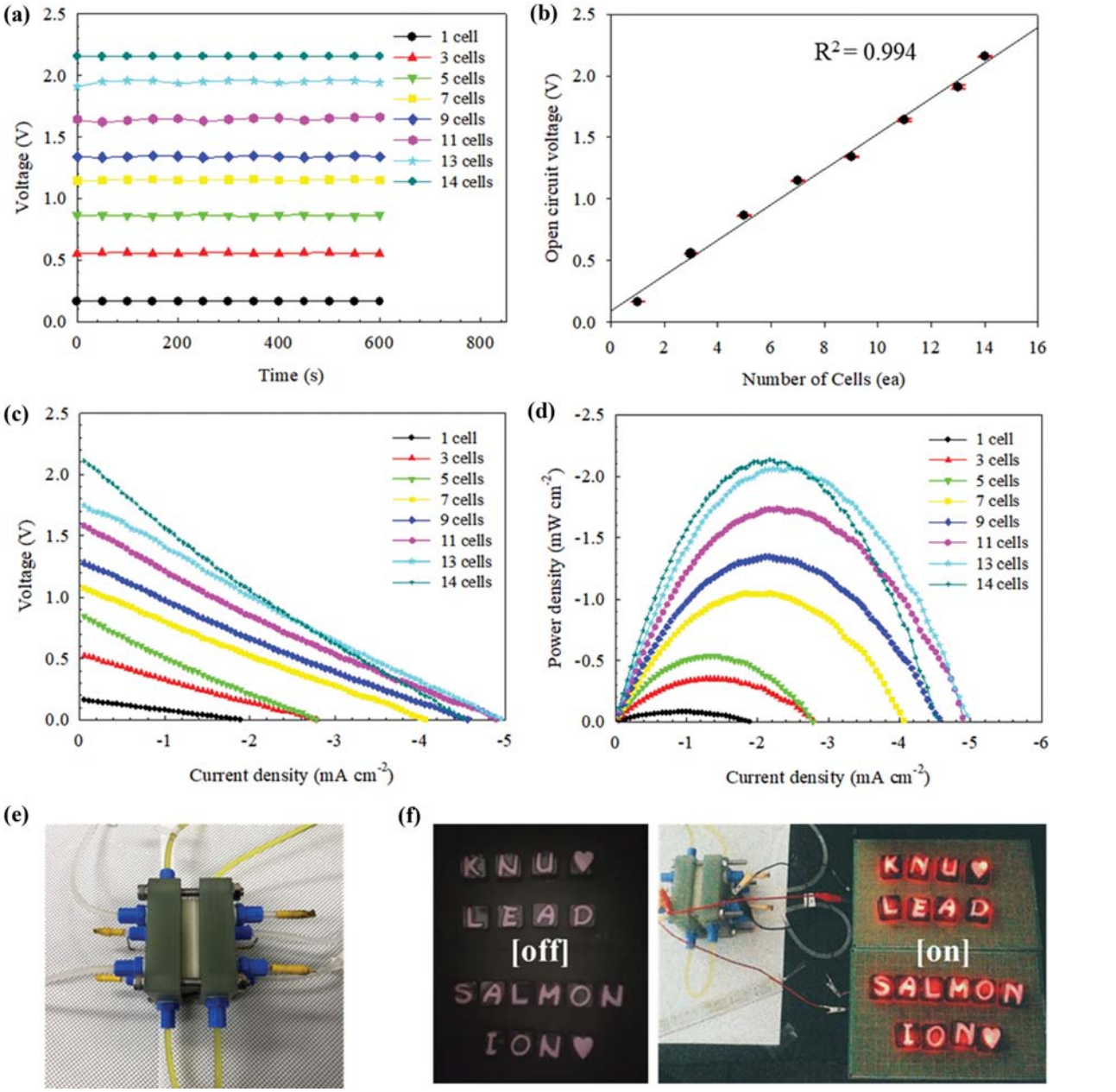

Fig. 8. Performance and power-generating demonstration of RED stack embedded with Pt/Ti mesh electrode: (a) monitoring OCV of RED stacks with different number of membrane pairs ((1-14) cells), (b) correlation of OCV with the number of cells, (c) j-V plots and (d) j-P curves of the RED stacks, (e) the assembled RED stack with 14 cells, and (f) lighting-up the LED lamps by electricity generated from the RED stack.

cells revealed that among the electrodes, Pt/Ti mesh electrode achieved the highest j_{max} (−16.13 A m^{-2}) and P_{max} (−0.702 W m^{-2}). The reduction in R_{cell} of the mesh-embedded RED cell compared to that of the foil-embedded one was mostly responsible for the drastic decrease in R_{HF} which was quantitatively supported by EIS analysis. The reduced R_{HT} from the mesh-type electrode was also attributed to an increase of active area, reflected by the capacitive behavior of the electrodes. The pure electrochemical activity of the electrode in converting ionic current to electric current was investigated by potentiodynamic sweep method, in which Pt/Ti mesh displays the exchange current density of (4.3 and 45.7) times greater than Ti mesh and Ti foil, respectively. These results imply that Pt/Ti mesh electrode induced small activation over-potential and small loss of energy. The durable and practical operation of the RED stack with Pt/Ti mesh electrode was demonstrated.

ACKNOWLEDGEMENTS

The research was funded by the Korea Electric Power Corporation (Grant number: R19XO01-02) and the Ministry of Science & ICT (NRF-2019R1I1A3A01063882). The study was also financially supported by 2018 Research Grant from Kangwon National Uni-

versity (No. 620180016).

REFERENCES

1. R. E. Pattle, *Nature*, **174**, 660 (1954).
2. S. Loeb and R. S. Norman, *Science*, **189**, 654 (1975).
3. S. Loeb, *J. Membr. Sci.*, **1**, 49 (1976).
4. T. Thorsen and T. Holt, *J. Membr. Sci.*, **335**, 103 (2009).
5. R. E. Pattle, *Chem. Prog. Eng.*, **35**, 351 (1955).
6. G. L. Wick and W. R. Schmitt, *Mar. Technol. Soc. J.*, **11**, 16 (1977).
7. J. W. Post, H. V. M. Hamelers and C. J. N. Buisman, *Environ. Sci. Technol.*, **42**, 5785 (2008).
8. J. Veerman, M. Saakes, S. J. Metz and G. J. Harmsen, *Chem. Eng. J.*, **166**, 256 (2011).
9. J. N. Weinstein and F. B. Leitz, *Science*, **191**, 557 (1976).
10. R. E. Lacey, *Ocean Engng.*, **7**, 1 (1980).
11. P. Dlugolecki, K. Nymeijer, S. J. Metz and M. Wessling, *J. Membr. Sci.*, **319**, 214 (2008).
12. J. Veerman, R. M. de Jong, M. Saakes, S. J. Metz and G. J. Harmsen, *J. Membr. Sci.*, **343**, 7 (2009).
13. D. A. Vermass, M. Saakes and K. Nijmeijer, *J. Membr. Sci.*, **385-386**, 234 (2011).
14. D. A. Vermass, M. Saakes and K. Nijmeijer, *J. Membr. Sci.*, **453**, 312 (2014).
15. E. Guler, R. Elizen, M. Saakes and K. Nijmeijer, *J. Membr. Sci.*, **458**, 136 (2014).
16. K. Kwon, S. J. Lee, L. Li, C. Han and D. Kim, *Int. J. Energy Res.*, **38**, 530 (2014).
17. J. G. Hong and Y. Chen, *J. Membr. Sci.*, **460**, 139 (2014).
18. E. Guler, Y. Zhang, M. Saakes and K. Nijmeijer, *ChemSusChem*, **5**, 2262 (2012).
19. P. Dlugolecki, A. Gambier, K. Nijmeijer and M. Wessling, *Environ. Sci. Technol.*, **43**, 6888 (2009).
20. D. A. Vermass, M. Saakes and K. Nijmeijer, *Environ. Sci. Technol.*, **45**, 7089 (2011).
21. P. Dlugolecki, J. Dabrowska, K. Nijmeijer and M. Wessling, *J. Membr. Sci.*, **347**, 101 (2010).
22. J. Balster, D. F. Stamatialis and M. Wessling, *J. Membr. Sci.*, **360**, 185 (2010).
23. D.-K. Kim, C. Duan, Y.-F. Chem and A. Majumdar, *Microfluid. Nanofluid.*, **9**, 1215 (2010).
24. J. Jagur-Grodzinski and R. Kramer, *Ind. Eng. Chem. Process. Des. Dev.*, **25**, 443 (1986).
25. M. Turek and B. Bandura, *Desalination*, **205**, 67 (2007).
26. J. Veerman, J. W. Post, M. Saakes, S. J. Metz and G. J. Harmsen, *J. Membr. Sci.*, **310**, 418 (2008).
27. J. Veerman, M. Saakes, S. J. Metz and G. J. Harmsen, *J. Appl. Electrochem.*, **40**, 1461 (2010).
28. O. S. Burheim, F. Seland, J. G. Pharoah and S. Kjelstrup, *Desalination*, **285**, 147 (2012).
29. O. Scialdone, C. Guarisco, S. Grispo, A. D. Angelo and A. Galia, *J. Electroanal. Chem.*, **681**, 66 (2012).
30. F. Suda, T. Matsuo and D. Ushioda, *Energy*, **32**, 165 (2007).
31. D. A. Vermass, S. Bajracharya, B. B. Sales, M. Saakes, B. Hamelers and K. Nijmeijer, *Energy Environ. Sci.*, **6**, 643 (2013).
32. I. Choi, J. Y. Han, S. J. Yoo, D. Henkensmeier, J. Y. Kim, S. Y. Lee, J. Han, S. W. Nam, H.-J. Kim and J. H. Jang, *Bull. Kor. Chem. Soc.*, **37**, 1010 (2016).
33. K. S. Kim, W. Ryoo, M.-S. Chun and G.-Y. Chung, *Desalination*, **318**, 79 (2013).
34. S. Pawlowski, J. G. Crespo and S. Velizarov, *J. Membr. Sci.*, **462**, 96 (2014).
35. D. A. Vermass, J. Veerman, N. Y. Yip, M. Elimelech, M. Saakes and K. Nijmeijer, *ACS Sustain. Chem. Eng.*, **1**, 1295 (2013).
36. L. Gurreri, A. Tamburini, A. Cipollina, G. Micale and M. Ciofalo, *J. Membr. Sci.*, **468**, 133 (2014).
37. M. Tedesco, A. Cipollina, A. Tamburini, I. D. L. Bogle and G. Micale, *Chem. Eng. Res. Des.*, **93**, 441 (2015).
38. M. Tedesco, A. Cipollina, A. Tamburini, W. van Baak and G. Micale, *Desalin. Water Treat.*, **49**, 404 (2012).
39. J. G. Hong, W. Zhang and Y. Chen, *Appl. Energy*, **110**, 244 (2013).
40. R. Audinos, *J. Power Sources*, **10**, 203 (1983).
41. H. Park, K. M. Kim, H. Kim, D.-K. Kim, Y. S. Won, and S.-K. Kim, *Korean J. Chem. Eng.*, **35**(7), 1547 (2018).
42. K. Zhou, C. Y. An, P. K. Kannan, N. Seo, Y.-S. Park and C.-H. Chung, *Korean J. Chem. Eng.*, **34**(5), 1483 (2017).
43. A. Daniilidis, D. A. Vermass, R. Herber and K. Nijmeijer, *Renew. Energy*, **64**, 123 (2014).
44. X. Zhu, W. He and B. E. Logan, *J. Membr. Sci.*, **494**, 154 (2015).
45. J -S. Park, J.-H. Choi, J.-J. Woo and S.-H. Moon, *J. Colloid Interface Sci.*, **300**, 655 (2006).
46. D. Quéré, *Annu. Rev. Mater. Res.*, **38**, 71 (2008).
47. S. J. Hitchcock, N. T. Carroll and M. G. Nicholas, *J. Mater. Sci.*, **16**, 714 (1981).